Microwave lymphedema assessment using deep learning with contour assisted backprojection

Yuyi Chang, Nithin Sugavanam, and Emre Ertin Department of Electrical and Computer Engineering
The Ohio State University
Columbus, OH 43210, USA
Email: chang.1560@osu.edu

Abstract—This paper presents a microwave imaging based method for detection of lymphatic fluid accumulation in lymphedema patients. The proposed algorithm uses contour information of the imaged limb surface to approximate the wave propagation velocity locally to solve the eikonal equation for implementing the adjoint imaging operator. This modified backprojection algorithm results in focused imagery close to the limb surface where lymphatic fluid accumulation presents itself. Next, a deep neural network based on U-Net architecture is employed to identify the location and extent of the lymphatic fluid. Simulation studies with various upper and lower arm profiles are used to compare the proposed contour assisted backprojection imaging with the baseline approach that assumes homogeneous media. The empirical results of the simulation experiments show that the proposed imaging method significantly improves the ability of the deepnet model to identify the location and the volume of the body fluid.

Index Terms—microwave imaging, lymphedema, tomographic imaging, bioelectromagnetics

I. INTRODUCTION

Lymphedema is a chronic and progressive disease caused by impaired lymphatic drainage. This disease is a disabling, painful, and disfiguring complication of nodal therapy for various cancer types, affecting roughly 2-3 million people in the United States alone, representing 10-30% of cancer survivors [1]. Various assessment methods for lymphedema are available in the clinical setting such as perometry, and other forms of limb volume assessment with limited utility for early detection or intervention. Microwave bio-radar sensing is an emerging non-invasive biosensing modality, which can be used to assess the dielectric properties of subcutaneous tissues. These sensors are low cost, easy to deploy, and applicable for both home and clinical care settings. However, inferring the dielectric properties of internal tissues from microwave measurements is an ill-posed inverse problem [2], [3]. The ill-conditioning of the forward operator is worsened it there exists an air gap between the antenna elements and the skin surface. As this leads to an abrupt change in relative permittivity from airskin interface and consequently a large reflection coefficient as compared to returns from internal tissues. Additionally, the transfer function of the antenna elements needs to be calibrated in situ, as it is uncertain when placed in close proximity of the body, increasing the number of parameters that needs to be estimated [3], [4].

A. Related works

Secondary lymphedema is a chronic and progressive disease caused by impaired lymphatic drainage, which results in the accumulation of interstitial protein-rich fluid and subsequent swelling of the limbs [5]. Existing medical imaging modalities like Magnetic Resonance Imaging (MRI) and X-ray can be used to detect abnormalities in the tissue structure with the use of contrast agents such as Indocyanine green [1]. The detection is accurate but the associated costs adversely increased the patients' burdens to receive proper healthcare.

Multiple studies have investigated the use of radiofrequency (RF) based sensors to detect stroke, detect brain tumor, and screen breast cancer [6]–[9] and established the efficacy of this modality in detecting permittivity changes. Existing work commonly assume that the antenna is well matched to the skin layer, which is achieved by optimizing the impedance of the antenna to match the tissue profile or by using an additional matching medium. Yet, this complicate the clinical implementation due to near field radiation and undermine patient comfort. Microwave imaging for lymphedema diagnostics have yet received much attention, with the only known study [10] focuses on antenna design perspective.

Deep learning have achieved state-of-the-art performances in many imaging tasks on both medical and natural image domains [11], [12]. Microwave imaging uses deep learning to facilitate reconstruction backscattered signals and identifying abnormal tissues in biosensing scenarios [13], [14]. Yet, the learning tasks typically focus on a narrow frequency, most limited by the antenna design, and are developed on limited datasets.

B. Contributions

In this paper, we develop a deep learning method that uses contour guided backprojection to precisely identify the presence of excess body fluid within the tissues. Rather than requiring a matching medium with controlled dielectric properties, we operate with air gap between the antennas and the body and assume that the surface contour of the imaged limb is available from a separate modality (e.g. stereo imaging, millimeter wave radar, etc). We use the contour information to create an approximate velocity map and employ a time domain backprojection technique tailored for heterogeneous media which leads to focused imagery close to the limb surface

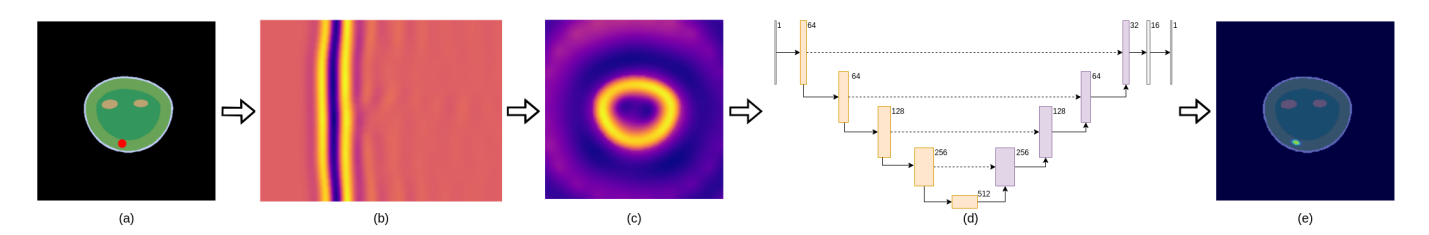


Fig. 1. Illustration of our methodology: (a) a limb profile that is being assessed for lymphedema, with accumulated body fluid denoted in red and is unknown to the model; (b) tomographic data $P_i(t), i = 1, 2, ..., M$ collected/simulated based on the limb profile; (c) Contour guided backprojection image $I(\vec{r})$; (d) deep learning U-Net model for localizing lymphedema; (e) model prediction of lymphatic fluid location superimposed on the limb profile.

where lymphatic fluid accumulation presents itself. We test the proposed algorithm with data from simulation experiments with various upper and lower arm profiles. Specifically, we pair a deep learning based detector with both the proposed contour assisted backprojection imaging method and the baseline approach that assumes homogeneous media, and compare lymphatic fluid detection performance using various metrics.

Our results show that the model can detect the presence and extent of lymphatic fluid better than the baseline approach that combines standard backprojection with a deep learning model.

This paper focuses specifically on identifying lymphedema, but the methodology is flexible on any segmentation problems presented in microwave biosensing (e.g., finding tumors/stroke), in which the cancerous/abnormal tissues have different EM permittivity profiles compared to other tissues.

II. COUNTER GUIDED TIME DOMAIN BACKPROJECTION ALGORITHM

We consider a circular radar array with M individual elements that operates in a monostatic transmit and receive setting sensing the spatial domain Ω . Each transceiver element comprising of a transmitter (TX) and a receiver (RX) element are spaced at a known distance d, taking M tomographic measurements around the limb equally spaced covering 360°. We further assume the surface contour of the limb is available from a secondary modality to provide an occupancy mask to guide the backprojection algorithm. In the following, we first review traditional time domain backprojection algorithm in a homogeneous medium based on the Time-of-Flight (ToF) calculations. Next, we present a contour guided locally interpolated (CGLI) backprojection approach that takes into account a spatially varying EM propagation speed by taking into consideration the tissue profile prior using fast marching method that uses local plane wave assumptions.

A. Review of time-domain backprojection in homogeneous medium

We consider a 2D spatial grid Ω containing M radar elements. Each element, indexed by i=1,...,M, is equipped with a transmitter TX at $\vec{T}_i \in \Omega$ and a receiver RX at $\vec{R}_i \in \Omega$. For any point $\vec{r}=(x,y)\in \Omega$, the travel time t_i to i^{th} radar element can be calculated by time-of-flight (ToF).

$$t_{i}(\vec{r}) = t_{T_{i}}(\vec{r}) + t_{R_{i}}(\vec{r})$$

$$= \frac{1}{v} \left(||\vec{T}_{i} - \vec{r}||_{2} + ||\vec{R}_{i} - \vec{r}||_{2} \right).$$
(1)

where $v=c/\sqrt{\epsilon}$ is the wave propagation speed determined by permittivity ϵ of the medium with respect to the speed of light in a vacuum c.

The radar system produces a series of tomographic measurements $P(t) = \{P_1(t), P_2(t), ..., P_M(t)\}$. We sample the backscattered received signal $P_i^S[m] = P_i(m \cdot \Delta t)$ at constant sampling interval Δt for m = 0, 1, ..., M. Signal contribution from the i^{th} transmit-receive pair $I_i(\vec{r})$ can be determined by interpolating $P_i(t)$ between t_k and $(t_k + \Delta t)$ where $t_k < t_i(\vec{r}) \le t_k + \Delta t$:

$$I_{i}(\vec{r}) = P_{i}(t_{k}) \cdot \frac{t_{i}(\vec{r}) - t_{k}}{\Delta t} + P_{i}(t_{k} + \Delta t) \cdot \frac{(t_{k} + \Delta t) - t_{i}(\vec{r})}{\Delta t}$$
(2)

The backprojected signal intensity, denoted as $I(\vec{r})$, is determined by the superposition of signals from all M transmitreceive pairs.

$$I(\vec{r}) = \sum_{i=1}^{M} I_i(\vec{r}) \tag{3}$$

B. Contour guided locally interpolated backprojection

We now examine the backprojection for the i^{th} tx-rx pair $P_i(t)$ in a heterogeneous medium with spatially varying permittivity. Wave propagation in this setup leads to multiple reflections due to the changing permittivity. More importantly, the wave velocity slows down due to increased permittivity in biological tissues resulting in increased spatial resolution when compared with free space propagation, thereby posing a challenge in identifying body fluid within internal tissues.

Given the i^{th} radar element, we start by creating a travel time map $\tau_{T_i}(\vec{r})$ and $\tau_{R_i}(\vec{r})$ that denotes the shortest propagation time to each point $\vec{r} = (x, y)$ in the scene originating from transmitter T_i and receiver R_i respectively.

Inspired by the success in tracing the travel wave in geoscience applications, we employ an Anisotropic Locally Interpolated Fast Marching Method (ALI-FMM) [15] to compute a 2D travel time in heterogeneous media. The algorithm utilizes

the velocity map of the propagation medium and iteratively calculates the total travel time from a starting point to all points on the spatial grid.

We find the shortest travel time by solving the eikonal equation given by

$$|\nabla \tau(\vec{r})| = \frac{1}{v(\vec{r}, \nabla \tau / |\nabla \tau|)} \tag{4}$$

subject to boundary conditions:

$$\tau_{T_i}(\vec{T_i}) = 0 \quad \tau_{R_i}(\vec{R_i}) = 0.$$
(5)

where $\tau(\vec{r})$ is the shortest travel path, and $v(\vec{r}, \nabla \tau / |\nabla \tau|)$ is the speed of the anisotropy media at point $\vec{r} = (x, y)$.

In this work, we consider biological tissues are isotropic [16]. The wave velocity at point \vec{r} is independent of the traveling directions and can be reduced to $v(\vec{r}, \nabla \tau/|\nabla \tau|) = v(\vec{r})$.

The travel time calculation is iterative starting from a source point \vec{T}_i or \vec{R}_i and propagate to all $\vec{r} \in \Omega$. Once the time travel maps $\tau_{T_i}(\vec{r})$ and $\tau_{R_i}(\vec{r})$ are determined, the total travel time map $t_i(\vec{r})$ is simply given by:

$$t_i(\vec{r}) = \tau_{T_i}(\vec{r}) + \tau_{R_i}(\vec{r}). \tag{6}$$

We solve the eikonal equation iteratively, by following the steps in [15] and introduce three states for any point to keep track of the progress of traversal: "known", "close", and "far". At the beginning, all points are initialized to "far" state where none of the point has been visited. The points are updated to "close" as soon as they have been traversed, indicating a middle state where a precise travel time has not been determined. Traversal to a point is considered completed when it becomes "known" state, meaning a travel time has been set after multiple optimization iterations. The iterations take a similar form as breadth-first search (BFS) search algorithm where the algorithm advances to the next closest spatial grid at each steps. However, in order to achieve a higher accuracy and to avoid quantization error, the methodology employs a collection of 32 stencils to better approximate traveling wavefront using locally linear wavefronts. This results in additional search steps to select a stencil that achieves the best approximation. Again the backprojected image $I(\vec{r})$ can be obtained by aggregating individual single images $I_i(\vec{r})$ following equation 2-3.

Fig. 2 illustrates individual steps to obtained a full backprojected image using CGLI method. A velocity map (Fig. 2(a)) is constructed based on arm occupancy information using an effective permittivity $\epsilon_{eff}=5$. The velocity map enables travel time $\tau(\vec{r})$ (Fig. 2(b)) calculation. Fig. 2(c) shows single angle backprojected image $I_i(\vec{r})$ by interpolating received signal $P_i(t)$ at the first radar element i=1. The final backprojected image $I(\vec{r})$ is obtained by repeating the previous steps for all 24 radar elements and aggregating the backprojection results (Fig. 2(d)).

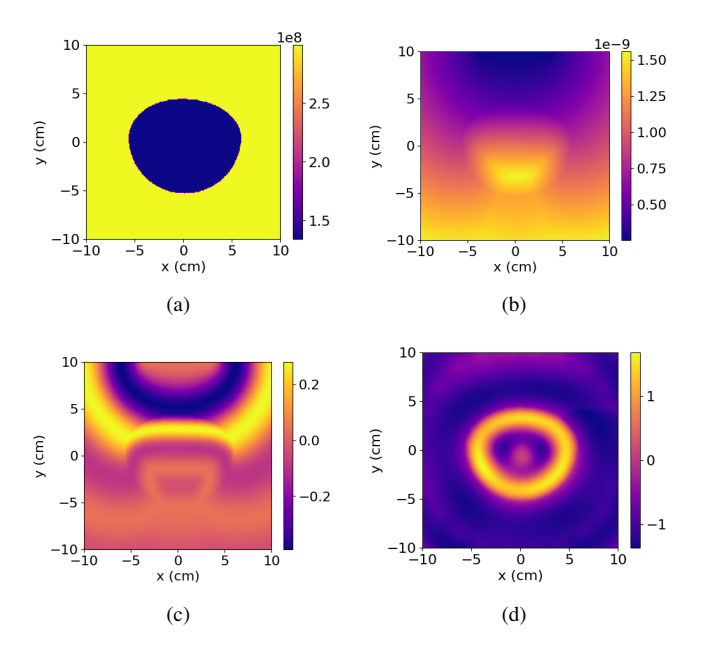


Fig. 2. Obtaining backprojected image $I(\vec{r})$ from collected measurements P(t) using CGLI backprojection method: (a) velocity map $v(\vec{r})$ constructed based on limb occupancy; (b) two way travel time $t_i(\vec{r}) = \tau_{T_i}(\vec{r}) + \tau_{R_i}(\vec{r})$; (c) backprojected image $I_i(\vec{r})$ from a single TX/RX Pair. (d) full backprojected image $I(\vec{r})$.

III. DEEP LEARNING MODEL

In this paper, we focus on a segmentation problem using a deep learning model designed to detect and localize lymphatic fluids. Using a backprojected image $I(\vec{r})$ as the input, the model produces a mask that contains probabilistic measurements ranged from 0 to 1 indicating the likelihood of a given pixel containing body fluid. The detection of an elevated presence of body fluid is indicative of lymphedema.

Our model is a deep convolutional neural network that is based on U-Net architecture [17]. The U-Net model is first introduced for medical image segmentation tasks, and its design has demonstrated robust performances for other computer vision problems across different domains [17], [18]. The architecture consists of an encoding path and a decoding path, forming a U-shape structure as shown in Fig. 3. Skip connections are placed between individual encoding and decoding levels in order to mitigate information loss during convolutional down/upsampling operations.

We follow the configuration as in the original U-Net model [17] to construct our model. Starting from a raw input image, the encoding path at every level condenses the input features to a higher-level description through multiple convolutional blocks. Each convolution block contains two sequentially operated 2D convolution, batch normalization and ReLU activation layers. At the end of each encoding level, the feature channel is doubled. An identical copy is cropped and passed through the skip connection to its corresponding decoder step, and a max pooling layer downsamples the original features by half for the next encoding step. At each decoding level on the decoding path, the skip connected features is concatenated with features

from previous step. The combined features are upsampled by a convolutional layer and processed by the convolutional blocks following the same setup as in the encoding path.

A final convolutional blocks contains a sigmoid layer, and is used to produce probability mask for localizing lymphatic fluid. Under binary segmentation formulation, the final sigmoid layer is typically combined into loss function for improved numerical stability. We further employ residual connections [19] on encoding path to promote network's ability to identifying underlining body fluid. This results a hybrid deep learning model based on U-Net architecture [17] for improved segmentation capacity.

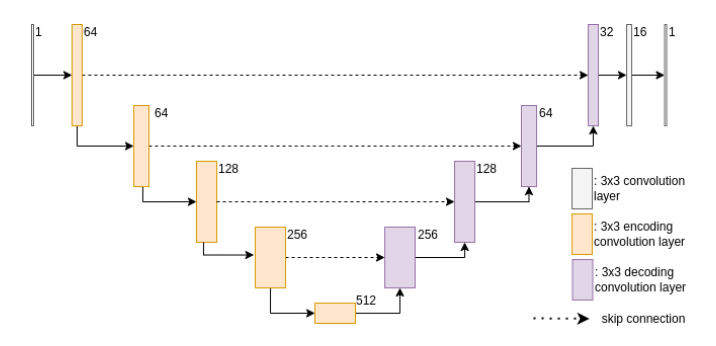


Fig. 3. Illustration of deep learning U-Net model. The model contains multiple 3x3 convolutional blocks designed to extract image features at different dimensions. The model has a encoding (orange blocks) and a decoding path (purple blocks) that performs convolutional down/upsampling, respectively. The skip connections (dashed line) form direct connections between encoding and decoding paths to mitigate information loss.

IV. EXPERIMENTS

A. Datasets

We constructed upper extremity phantoms based on measurements from typical healthy adults. Ten base phantoms were generated, each incorporating layers representing skin, fat, muscle and bone tissues. A cylindrical shape body fluid object is introduced within the fat layer mimicking the presence of lymphedema. The severity of lymphedema was controlled by varying the radius of the body fluid object.

EM backscattered data were obtained through FDTD simulations using gprMax software [20]. A tomography scan comprised samples taken at 24 uniformly spaced angles with a 20 x 20 cm domain. The simulation utilized a built-in bowtie antenna, operating at 1.5 GHz with an approximate 1 GHz bandwidth. Calibration to simulated data was performed involving aligning time axis using a set of size varying PEC cylinders, and free space calibration to enable coherently subtract antenna effects.

The EM dataset contain 676 samples which corresponds to 16224 individual simulations. We performed a random split of the dataset based on phantom profiles into training, validation and testing datasets. The distribution of samples is as follows: 520 samples for training, 52 samples for validation, and 104 samples for testing.

EM simulations are inherently CPU intensive and time consuming tasks, making it crucial to accelerate data generations to support data driven methods. We leverage GPU accelerated computing by offloading CPU tasks to multiple GPUs. A load balancing application was built to support executing a simulation task pool across multiple GPUs. This resulted approximately an 80x acceleration compared to running solely on CPU.

B. Implementation details

Backprojected images take the shape of 256x256 with a single pixel representing roughly 0.78x0.78 mm grid in spatial domain. A min/max scaling is applied to all resulting images to have min/max values set to in between 0 to 1. This ensure our received signals are always up to scale.

PyTorch framework is used for training and testing lymphedema segmentation. The training and testing are performed on a single Nvidia Quadro RTX 6000 GPU and Intel Xeon CPU server. The training data are augmented through random rotation and flipping. Our U-Net model contains five encoding/decoding steps, compressing the input feature up to 512 channels as shown in Fig. 3. We use pretrained ResNet-34 [19] as the backbone for U-Net encoders. The model takes single channel backprojected image as input and produces a single channel output. A sigmoid layer is applied the model output to produce probability map of body fluid. Binary cross entropy (BCE) loss is used for training between the output and ground truth segmentation masks. The model is trained 200 epochs, and the model weights that achieve the lowest validation loss is used for further evaluation.

C. Evaluation metrics

We evaluate our methodology by comparing segmentation performance to the non-contour assisted backprojection algorithm (Section II-A) using our test dataset. In addition to BCE test losses, we analyze the sensitivity of the models based on probability of detection P_D and probability of false alarm P_{FA} from receiver operating characteristic (ROC) curves. The ideal threshold setting for segmenting lymphatic fluid is determined by fixing a P_{FA} . We further analyze the model performances by the F1 and the intersection over union (IoU) scores:

$$F1 = \frac{TP}{TP + 0.5(FP + FN)} \tag{7}$$

$$IoU = \frac{TP}{(TP + FP + FN)}.$$
 (8)
V. RESULTS

A. Backprojection using different strategies

Fig. 4 presents single angle backprojected image $I_i(\vec{r})$ using ToF method (Fig. 4(a)) ad our CGLI method (Fig. 4(b)). To better understand the effects of backprojecting in a heterogeneous medium, a vertical slice is taken at the center of Fig. 4(b) to show the progression of backprojected signal intensity at the imaging plane that is orthogonal to the radar (Fig. 4(d)). We examine the relationships between the sliced backprojection and the original received signal (Fig. 4(c)). The red dashed lines on each sides of the two images indicate the duration

of backprojected time range. The orange and green markers indicate the duration during which the backprojected signal is within the phantom boundary. Between the two range markers, we can clearly see the signal presented in Fig. 4(d) appeared to be the stretched version compared to original signal in Fig. 4(c) due a slower propagation speed happening within the tissue. In addition, the effects of shadowing were observed where a mirrored copies of the original signals appear in the backprojected image. The shadowing occurs due to EM wave travel times are the same when penetrating the limb and travel along the air-skin interface before entering the internal tissues. Highlighted in purple, the local minima around 150 and 180 in Fig. 4(d) are symmetric around the purple marker in Fig. 4(c) at the lower regime of the phantom, which is also evident by examining the total travel time map (Fig. 2(b)) by drawing equal travel time contours. The effect is predominant due to skin effects during EM wave propagation [21]. However, the effect do not contribute significantly to the backprojected results as the shadowing effects only occur in the lower regime of the lime when the backscattered signal intensity is low.

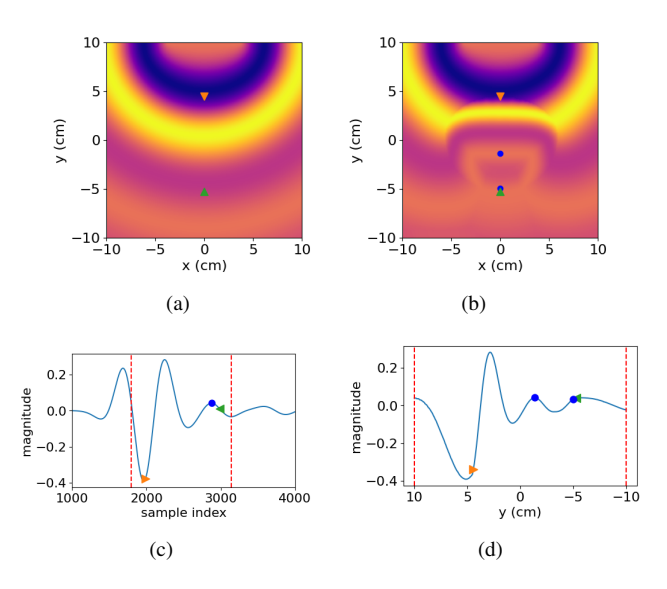


Fig. 4. Comparing backprojected image $I_i(\vec{r})$ obtained from a single angle using (a) ToF based backprojection and (b) our CGLI backprojecting methodology. (c) Original received signal $P_i(t)$ shown to compared with (d) a vertical cut showing progression of backprojected intensity. The triangular markers show the backprojected signal is within the tissue boundary. The circle markers highlights the dual local maxima as a result of shadowing.

B. Lymphedema segmentation using deep learning models

We now present deep learning results for identifying lymphatic fluid within the tissues using a U-Net model. Fig 5 presents the receiver operating characteristic (ROC) curves showing probability of detection P_D with respect to false alarm probability P_{FA} . The result shows our model achieves better detection accuracy compared to two baselines with different permittivity assumption under a fixed P_{FA} . At $P_{FA}=10^{-3}$, the detection probability of our model is $P_D=0.85$ over baselines' 0.32 and 0.20. We bias the model at $P_{FA}=10^{-3}$ and evaluate F1 score and IoU, in

addition to BCE loss reported during testing, as presented in Table I. Having the lowest testing BCE loss, our contour guided backprojection method continue to achieves strong performance over other baseline models with F1 score of 0.565 and IoU of 0.393.

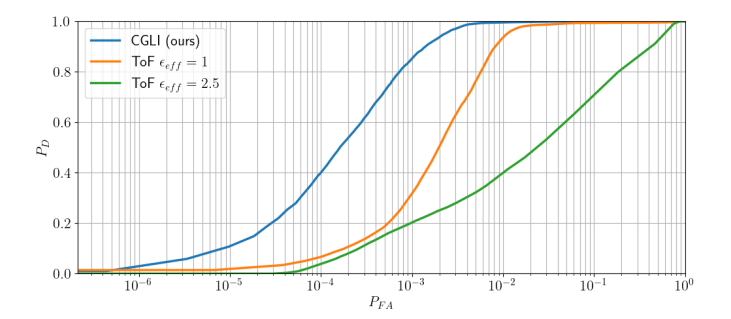


Fig. 5. Reciver operating characteristics (ROC) of our method and baseline models showing probability of detection P_D and probability of false alarm P_{FA} .

TABLE I
TEST RESULTS BASED ON BACKPROJECTION METHOD

Backprojection Method	BCE loss	F1 Score	IoU
ToF Baseline 1 ($\epsilon_{eff} = 2.5$)	0.00546	0.171	0.094
ToF Baseline 2 ($\epsilon_{eff} = 1.0$)	0.00328	0.255	0.146
Contour guided (CGLI)	0.00145	0.565	0.393

In the following we use two of the individual test samples to demonstrate the effectiveness of the proposed method over the alternative baseline methods discussed above in Fig. 6. The first test sample shows a lower limb with lymphatic fluid radius r = 2.5 mm, representing a mild state of lymphedema where a just-in-time intervention is necessary (Fig. 6(a)). The second test sample comes from a upper limb profile with a severe state of lymphedema at radius r = 6 mm (Fig. 6(b)). From top to bottom, we present 1) logit outputs from deep learning models, 2) predicted probability mask after the sigmoid of the final layer, and 3) predicted lymphedema location superimposed on the ground truth profile. Compared to baseline method with either permittivity assumption, our method precisely locate the location of lymphatic fluid on the phantom with less false positive. With contour guided methodology, the target location is already aligned with actual geometry, so no additional calibration needs to be learned by the U-Net to establish the transformation between the lymphatic fluid location in microwave imaging domain to spatial domain.

VI. CONCLUSION

In this paper, we presented a contour based backprojection imaging method when paired with a deep learning network can localize lymphedema present subcutaneously. We use prior information about the surface contour of the limb to to backproject received signals to spatial domain accounting different propagation speed inside and outside of the limb profile. The identification of lymphatic fluid is enabled by

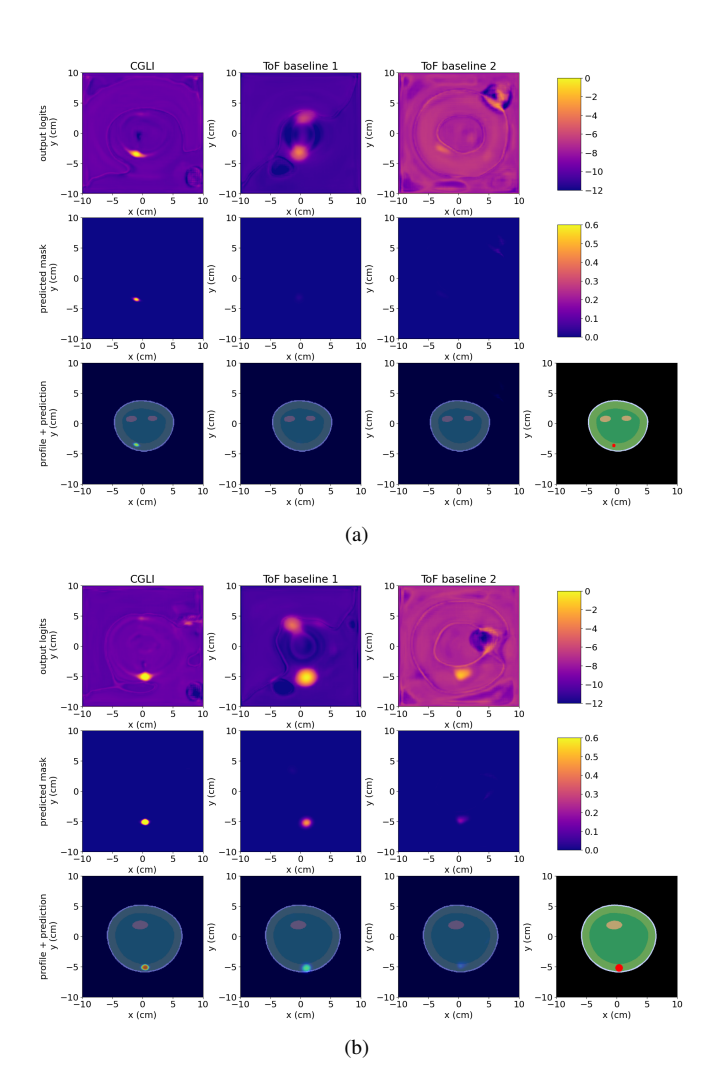


Fig. 6. Individual test samples comparing our method to baseline methods (left to right columns). On each subplot, intermediate model outputs including logits (row 1) and prediction probability map (row 2) are presented with assessment output superimposed on the ground truth profile (row 3). Our model shows confident and accurate predictions on (a) a lower limb with mild lymphedema $r=2.5 \, \mathrm{mm}$, and (b) a upper limb showing severe lymphedema $r=6 \, \mathrm{mm}$ compared to baseline methods.

a deep learning segmentation U-Net model, which takes the backprojected image and produces a probability map where the fluid may be presented on the phantom profile. We evaluated our methodology on a synthetic microwave imaging dataset and compared our method to baseline method. For future work, we will 1) develop a model that can infer and segment further subcutaneous structures like fat tissue, 2) expand our dataset to include a more diverse set of lymphatic fluid composition, and 3) evaluate on other existing microwave imaging datasets. We will make the model and the imaging code publicly available to facilitate microwave bio-imaging research.

ACKNOWLEDGMENT

This work is partly supported by NSF Grant CBET-2037398 and NIH Grant P41EB028242.

REFERENCES

- [1] J. C. Rasmussen, I.-C. Tan, M. V. Marshall, K. E. Adams, S. Kwon, C. E. Fife, E. A. Maus, L. A. Smith, K. R. Covington, and E. M. Sevick-Muraca, "Human lymphatic architecture and dynamic transport imaged using near-infrared fluorescence," *Translational Oncology*, vol. 3, no. 6, pp. 362–IN7, 2010.
- [2] D. W. Winters, E. J. Bond, B. D. Van Veen, and S. C. Hagness, "Estimation of the frequency-dependent average dielectric properties of breast tissue using a time-domain inverse scattering technique," *IEEE Transactions on Antennas and Propagation*, vol. 54, no. 11, pp. 3517–3528, 2006.
- [3] B. C. Civek and E. Ertin, "Bayesian sparse blind deconvolution using MCMC methods based on normal-inverse-gamma prior," *IEEE Transactions on Signal Processing*, vol. 70, pp. 1256–1269, 2022.
- [4] Y. Chang, N. Sugavanam, and E. Ertin, "Removing antenna effects using an invertible neural network for improved estimation of multilayered tissue profiles using UWB radar," in 2023 IEEE USNC-URSI Radio Science Meeting (Joint with AP-S Symposium). IEEE, 2023, pp. 53– 54.
- [5] A. K. Greene, "Epidemiology and morbidity of lymphedema," in *Lymphedema*. Springer, 2015, pp. 33–44.
- [6] S. Y. Semenov, D. R. Corfield et al., "Microwave tomography for brain imaging: Feasibility assessment for stroke detection," *International Journal of Antennas and Propagation*, vol. 2008, 2008.
- [7] M. Hopfer, R. Planas, A. Hamidipour, T. Henriksson, and S. Semenov, "Electromagnetic tomography for detection, differentiation, and monitoring of brain stroke: A virtual data and human head phantom study." *IEEE Antennas and Propagation Magazine*, vol. 59, no. 5, pp. 86–97, 2017
- [8] G. N. Bindu, S. Abraham, A. Lonappan, V. Thomas, C. Aanandan, and K. Mathew, "Active microwave imaging for breast cancer detection," *Progress In Electromagnetics Research*, vol. 58, pp. 149–169, 2006.
- [9] A. T. Mobashsher, A. Mahmoud, and A. Abbosh, "Portable wideband microwave imaging system for intracranial hemorrhage detection using improved back-projection algorithm with model of effective head permittivity," *Scientific reports*, vol. 6, no. 1, p. 20459, 2016.
- [10] D. Russo, "Preliminary investigation on microwave sensing for early detection of lymphoedema," Ph.D. dissertation, Politecnico di Torino, 2021
- [11] S. K. Zhou, H. Greenspan, C. Davatzikos, J. S. Duncan, B. Van Ginneken, A. Madabhushi, J. L. Prince, D. Rueckert, and R. M. Summers, "A review of deep learning in medical imaging: Imaging traits, technology trends, case studies with progress highlights, and future promises," *Proceedings of the IEEE*, vol. 109, no. 5, pp. 820–838, 2021.
- [12] J. Chai, H. Zeng, A. Li, and E. W. Ngai, "Deep learning in computer vision: A critical review of emerging techniques and application scenarios," *Machine Learning with Applications*, vol. 6, p. 100134, 2021.
- [13] W. Shao and Y. Du, "Microwave imaging by deep learning network: Feasibility and training method," *IEEE transactions on antennas and propagation*, vol. 68, no. 7, pp. 5626–5635, 2020.
- [14] B. Gerazov and R. C. Conceicao, "Deep learning for tumour classification in homogeneous breast tissue in medical microwave imaging," in *IEEE EUROCON 2017-17th International Conference on Smart Technologies*. IEEE, 2017, pp. 564–569.
- [15] J. Ludlam, K. Tant, V. Dolean, and A. Curtis, "Travel times and ray paths for acoustic and elastic waves in generally anisotropic media," *Journal of Computational Physics*, vol. 494, p. 112500, 2023.
- [16] X. Zhang, S. Zhu, and B. He, "Imaging electric properties of biological tissues by RF field mapping in MRI," *IEEE transactions on medical* imaging, vol. 29, no. 2, pp. 474–481, 2010.
- [17] O. Ronneberger, P. Fischer, and T. Brox, "U-net: Convolutional networks for biomedical image segmentation," in *Medical Image Computing* and Computer-Assisted Intervention–MICCAI 2015: 18th International Conference, Munich, Germany, October 5-9, 2015, Proceedings, Part III 18. Springer, 2015, pp. 234–241.
- [18] V. Khoshdel, M. Asefi, A. Ashraf, and J. LoVetri, "Full 3d microwave breast imaging using a deep-learning technique," *Journal of Imaging*, vol. 6, no. 8, p. 80, 2020.
- [19] K. He, X. Zhang, S. Ren, and J. Sun, "Deep residual learning for image recognition," in *Proceedings of the IEEE conference on computer vision* and pattern recognition, 2016, pp. 770–778.

- [20] C. Warren, A. Giannopoulos, and I. Giannakis, "gprMax: Open source software to simulate electromagnetic wave propagation for ground penetrating radar," *Computer Physics Communications*, vol. 209, pp. 163–170, 2016.
- [21] A. Vander Vorst, A. Rosen, and Y. Kotsuka, RF/microwave interaction with biological tissues. John Wiley & Sons, 2006.